Journal of
Composites Science

Article

Thermal Analysis of Crosslinking Reactions in Epoxy Nanocomposites Containing Polyvinyl Chloride (PVC)-Functionalized Nickel-Doped Nano-Fe_3O_4

Maryam Jouyandeh [1], Mohammad Reza Ganjali [1,2,*], Zohre Karami [1], Morteza Rezapour [3], Babak Bagheri [4], Payam Zarrintaj [5], Arash Mouradzadegun [6], Sajjad Habibzadeh [7] and Mohammad Reza Saeb [1,*]

[1] Center of Excellence in Electrochemistry, School of Chemistry, College of Science, University of Tehran, Tehran 11155-4563, Iran; maryam.jouyande@gmail.com (M.J.); zohrekarami.2013@yahoo.com (Z.K.)
[2] Biosensor Research Center, Endocrinology and Metabolism Molecular-Cellular Sciences Institute, Tehran University of Medical Sciences, Tehran 11155-4563, Iran
[3] IP Department, Research Institute of Petroleum Industry (RIPI), Tehran P.O. Box 14665-137, Iran; rezapourm@ripi.ir
[4] Department of Chemical and Biomolecular Engineering, Korea Advanced Institute of Science and Technology (KAIST), Daejeon 34141, Korea; babakbagheri@kaist.ac.kr
[5] School of Chemical Engineering, Oklahoma State University, 420 Engineering North, Stillwater, OK 74078, USA; payam.zarrintaj@okstate.edu
[6] Department of Chemistry, Faculty of Science, Shahid Chamran University of Ahvaz, Ahvaz 61357-43311, Iran; arash_m@scu.ac.ir
[7] Department of Chemical Engineering, Amirkabir University of Technology (Tehran Polytechnic), Tehran 1591639675, Iran; sajjad.habibzadeh@aut.ac.ir
* Correspondence: ganjali@ut.ac.ir (M.R.G.); mrsaeb2008@gmail.com (M.R.S.)

Received: 16 June 2020; Accepted: 31 July 2020; Published: 5 August 2020

Abstract: This work reports on the thermal analysis of epoxy containing polyvinyl chloride (PVC) surface-functionalized magnetic nanoparticles (PVC–S/MNP) and its bulk-modified nickel-doped counterpart (PVC–S/MNP/Bi–B). Nanoparticles were synthesized through the cathodic electro-deposition method. The morphology of particles was imaged on a field-emission scanning electron microscope (FE-SEM), while X-ray diffraction analysis and Fourier-transform infrared spectroscopy (FTIR) were used to detect changes in the structure of nanoparticles. The magnetic behavior of particles was also studied by vibrating sample magnetometry (VSM). In particular, we focused on the effect of the bulk (Ni-doping) and surface (PVC-capping) modifications of MNPs on the thermal crosslinking of epoxy using nonisothermal differential scanning calorimetry (DSC) varying the heating rate. The cure labels of the prepared nanocomposites were assigned to them, as quantified by the cure index. The good cure state was assigned to the system containing PVC–S/MNP/Bi–B as a result of excessive ring opening of epoxy. Cure kinetics parameters of PVC–S/MNP/Bi–B incorporated epoxy was obtained by the use of isoconversional methodology. The activation energy of epoxy was decreased upon addition of 0.1 wt% of PVC–S/MNP/Bi–B due to the reaction of Cl^- of PVC by the functional groups of resin.

Keywords: crosslinking; surface functionalization; cure index; epoxy; cure kinetics

---

1. Introduction

Epoxy resins have widely been applied in technological fields because of their promising physical and mechanical [1], adhesion [2,3], flame retardant [4] and anti-corrosion [5] properties. The physicochemical properties achieved by the combination of inorganic nanoparticles and organic epoxy give rise to the properties superior to the neat epoxy. Various nanostructured materials including carbon nanotubes [6], graphene oxide [7], nanoclay [8], silica [9], halloysite nanotubes [10], layered double hydroxides [11–13], metal organic frameworks [14,15] and iron oxide nanoparticles [16,17] have been incorporated into epoxy resin to introduce new features to the epoxy, such as electrical and thermal conductivity, magnetic properties and thermomechanical properties. Magnetic nanoparticles (MNPs) have been synthesized and incorporated into the epoxy matrix for improving their thermal, mechanical, anti-corrosion and electrical properties [18,19].

The insoluble and infusible epoxy would be the result of the crosslinking reaction of liquid prepolymers with curing agents. Epoxy prepolymers participate in crosslinking reactions with a wide range of chemicals under various curing conditions, which severely affects the properties of the final epoxy finish [20]. The ultimate properties of MNP/epoxy nanocomposites strongly depend on the crosslinking state and the interaction between the epoxy and MNPs. A difficulty in preparation of epoxy nanocomposite containing MNPs is their high tendency for agglomeration. Metal ions doped and polymer coated MNPs are the solutions to tackle such a problem; so that, Mn^{2+} [21] and Zn^{2+} [22] doped in Fe_3O_4 nanoparticles were found to take position in either the bulk or the outermost layers of the crystalline zones. For Zn, Mn, Co and Gd dopants, the change in the energy of interaction is not monotonic. In fact, there are two kinds of Fe ions with different coordinates, i.e., Fe^{2+} and Fe^{3+} in the bulk layers of Fe_3O_4. Furthermore, the three-coordinated Fe ions are formed on the surface because of the existence of the dangling bonds. For that reason, three types of Fe ions exist in the Fe_3O_4 structure. The three-coordinated Fe ion locates on the surface, six-coordinated Fe ion stays in the subsurface and the 3rd layer contains four-coordinated Fe ions [23]. The Ni and Zn dopant tend to locate on the surface, while Co, Mn and Zn prefer to form subsurface doping. The effects of surface dopants on the reactivity of particle are higher than the interior dopants. Therefore, Ni dopant can improve the surface activity of Fe_3O_4. By doping Fe_3O_4 nanoparticles with Mn^{2+} and Zn^{2+}, less active sites in the bulk are formed compared to the surface of pristine Fe_3O_4 that causes deagglomeration. In addition, Mn^{2+} and Zn^{2+} known as Lewis acids can catalyze epoxy ring opening, which changes the label of cure of epoxy from poor to excellent, as unveiled by the cure index (*CI*). In contrast, a poor cure state was the consequence of doping Fe_3O_4 nanoparticles with Ni^{2+} dopants [24]. The Ni^{2+} dopants on the top layers of nano–Fe_3O_4 crystal dramatically increased the activity of MNPs surface, allowing MNPs for agglomeration. It was reported that gadolinium (Gd)-doped Fe_3O_4 nanoparticles improve the crosslinking of epoxy by substituting Fe^{3+} with Gd^{3+} [25]. In addition, it was found that curing reactions taking place between the epoxy and amine curing agent are intensified by the introduction of Fe_3O_4 nanoparticles doped with Co^{2+} [26], because of replacing Fe^{2+} in the bulk layers by the Co^{2+} deagglomeration. Moreover, it is reported that surface functionalization of MNPs with various functional groups such as polyvinylpyrrolidone [27–29], ethylenediaminetetraacetic acid [30] and polyethylene glycol [31–33] facilitates the crosslinking of epoxy by improving the dispersibility of nanoparticles.

In this work, three types of MNPs including naked MNPs, polyvinyl chloride surface functionalized MNPs (PVC–MNPs) and Ni^{2+}-doped PVC–MNPs were compared for their effects on crosslinking of epoxy. The synthesized MNPs were analyzed for chemical structure with X-ray diffraction (XRD) and Fourier-transform infrared spectroscopy (FT-IR). The morphology and the magnetic properties of nanoparticles were studied by field-emission scanning electron microscopy (FE-SEM) and vibrating sample magnetometry (VSM), respectively. The effect of PVC–MNPs and Ni^{2+}-doped PVC–MNPs on the curability of epoxy nanocomposites was monitored using nonisothermal analyses made by differential scanning calorimetry (DSC) in terms of the *CI*. Moreover, the cure kinetics of epoxy systems was studied using isoconversional methods.

2. Experimental

2.1. Materials

Polyvinyl chloride (PVC, $(C_2H_3Cl)_n$, Mw ~233,000), iron(II) chloride $4H_2O$ (Merck, 99.5%), iron (III) nitrate $9H_2O$ (Merck, 99.9%) and nickel nitrate $4H_2O$ (Merck, 99.5%) were used without further purification. Epon-828 with an average epoxide equivalent weight of 188 g/eq. was used as resin, while triethylenetetramine (TETA) with hydrogen equivalent weight of 25 g/eq. was used as curing agent. Both resin and curing agents were provided by Hexion Co., Ohio, USA.

2.2. Methods

Surface and bulk/surface modified PVC–MNP and Ni-doped PVC–MNP were synthesized based on a well-documented procedure used in previous works [34–36]. Figure 1 gives a general view of the bulk and surface modification of MNPS applied in this work. The electrochemical cell was composed of a cathode of steel 316 L sheet sandwiched between two anodes of steel 316L having surface area of 100 cm^2. The distance between the anode and the cathode electrodes was fixed at 5 cm. A mode of DC deposition with an identical current density of 10 $mA.cm^{-2}$ and deposition time of 30 min was also used in the synthesis of samples. The only variable was the composition of deposition bath. For PVC–MNPs, the deposition bath contained 2 g $Fe(NO_3)_3$, 0.3 g PVC and 1 g $FeCl_2$ dissolved in 1 L H_2O, while for the electrochemical deposition of Ni^{2+}-doped PVC–MNPs 2 g $Fe(NO_3)_3$ together with 1 g $FeCl_2$ and 0.3 g $Ni(NO_3)_2$ were dissolved in 1 L distilled water. The oxide films of PVC–MNPs and Ni^{2+}-doped PVC–MNPs were deposited when the applied current passed across the bath. Lastly, black films were appeared on the steel cathodes indicating successful synthesis of nanoparticles. These black films were then washed with ethanol and repeatedly washed with water. In the final step, the wet powders were heated at 70 °C for 1 h and the dried powders were labeled PVC–MNPs and Ni-doped PVC–MNPs and used in further analyses and experiments.

Epoxy nanocomposite were prepared based on 0.1 wt% PVC–MNPs or Ni-doped PVC–MNPs nanoparticles and epoxy under sonication with on–off cycle for 5 min. The mechanical mixer working at 2500 rpm further homogenized the dispersions for 15 min. The resin/hardener ratio was stoichiometrically adjusted by adding 13 wt% of TETA to the epoxy resin.

The surface morphology of MNPs was imaged on FE-SEM instrument (Mira 3-XMU, accelerating voltage of 100 kV). The change in chemical structure of MNPs was assessed using XRD patterns provided from MNPs conducted on a PW-1800 X-ray diffraction with a Co Kα radiation. Magnetic behavior of MNPs was monitored in between −20,000 and 20,000 Oe at RT condition by using a vibrational sample magnetometer (VSM, Meghnatis Daghigh Kavir Co., Iran). The FT-IR spectra of the prepared MNPs were acquired using Bruker Vector 22 IR instrument.

Nanocomposites containing 0.1 wt% PVC–MNPs and Ni-doped PVC–MNPs were analyzed for crosslinking behavior and kinetics applying nonisothermal tests on a PerkinElmer DSC 4000. Nonisothermal DSC was detected over a temperature range of 25–200 °C at different heating rates (β) of 5, 10, 15, 20 °C min^{-1}, under neutral atmosphere of nitrogen with a circulation rate of 20 $mL.min^{-1}$.

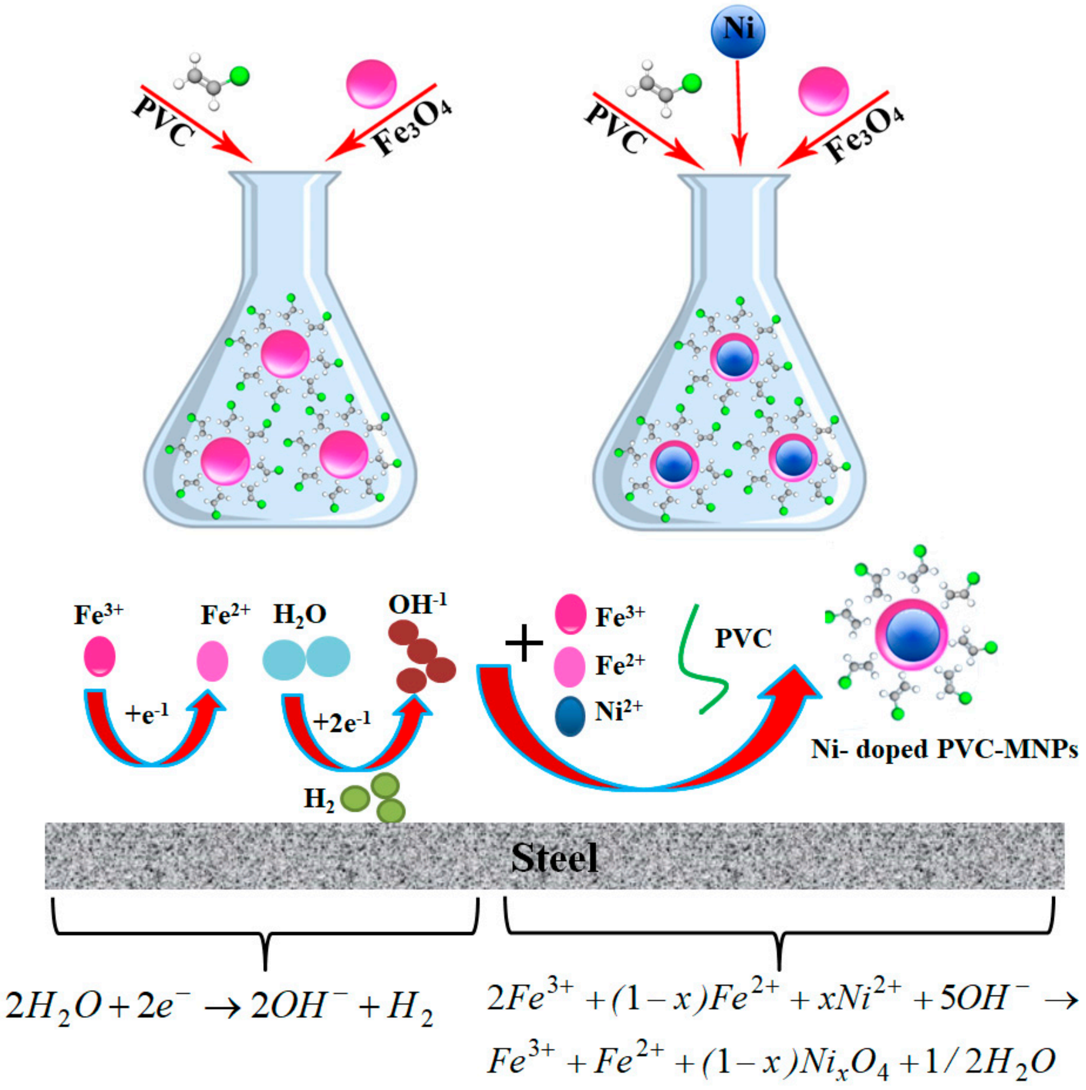

Figure 1. Surface and bulk modification of the Fe_3O_4 nanoparticles by the polyvinyl chloride (PVC) and Ni, respectively.

3. Results and Discussion

3.1. Structure and Morphology

The XRD patterns of the obtained MNPs are shown in Figure 2. In these patterns, the XRD peaks of (111), (220), (311), (400), (422), (511), (440) and (533) observed at 2θ of 10–80 were excellently confident with the peaks of the pure iron oxide with magnetite crystal structure (JCPDS number of 01–074–1910). These patterns have all peaks reported for the cubic magnetite in literature [37–40]. The average size of the crystalline domains (D) of the PVC–MNPs and Ni-doped PVC–MNPs was calculated to be 18.1 nm and 19.8 nm, respectively.

In comparing the XRD patterns of PVC–MNPs and PVC/Ni-doped MNPs, no distinguished shift in the position of peaks was observed. Since Ni^{2+} and Fe^{2+} cations have the same radius of about 0.7 Å, in the cubic crystal lattice of the bare Fe_3O_4, the octahedral sites are solely occupied with Fe(III) cations, while Fe(II) and Fe(III) cations are in the two tetrahedral sites. The Fe(II) cations in the Fe_3O_4 structure are replaced by the Ni^{2+} cations [34]. In the surface treatment, the PVC was added to the electrodeposition solution or electrolyte, hence, did not contribute to the electrochemical reactions occurring on the cathode electrode. After the nucleation and growth of Fe_3O_4 particles on the cathode electrode were completed, the surface was in situ capped by the PVC molecules. Therefore, Ni^{2+} doping into Fe_3O_4 and its surface modification by PVC had no essential effect on the XRD pattern and also the crystalline structure of iron oxide.

Figure 3 shows the FE-SEM micrographs provided from the surface of MNPs, where a spherical shape can be obviously observed for MNPs having an average size of ~20 nm [35,36]. Some aggregates are partially observed after Ni doping. Since the Ni dopant tends to locate on the surface of Fe_3O_4, it can improve the surface activity of nanoparticle. Evidently in Figure 3b, the higher surface activity of Ni-doped MNPs increases their tendency to agglomerate.

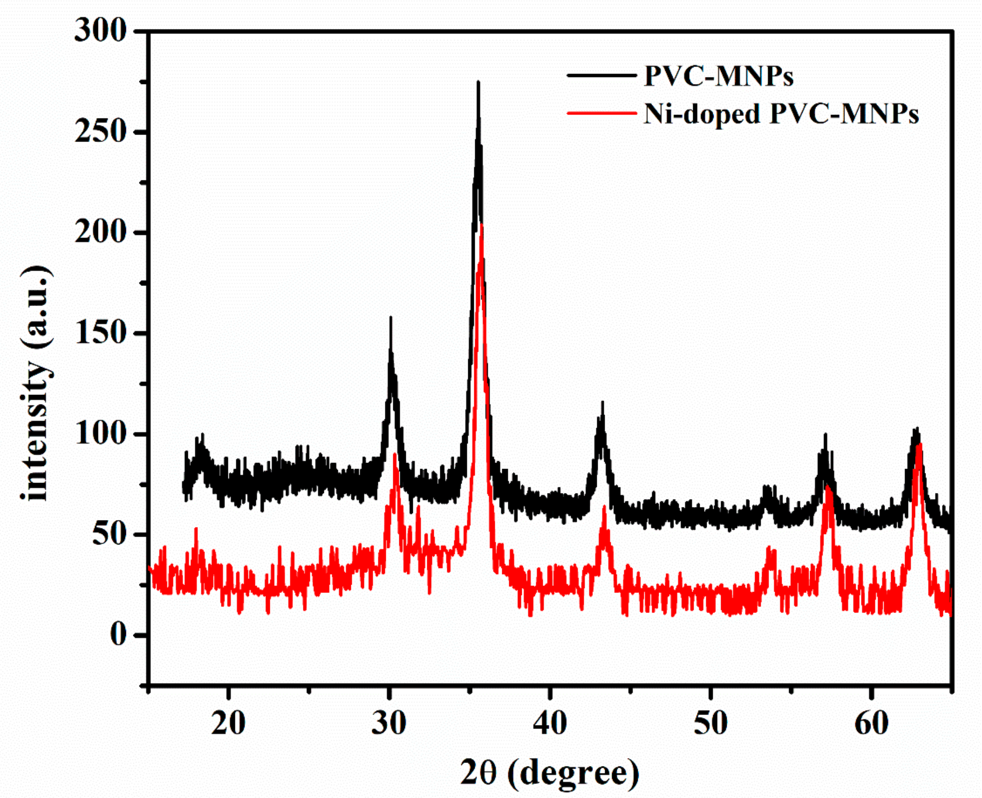

Figure 2. XRD patterns of the synthesized polyvinyl chloride (PVC) surface-functionalized magnetic nanoparticles (PVC-MNPs) and Ni-doped PVC–MNPs.

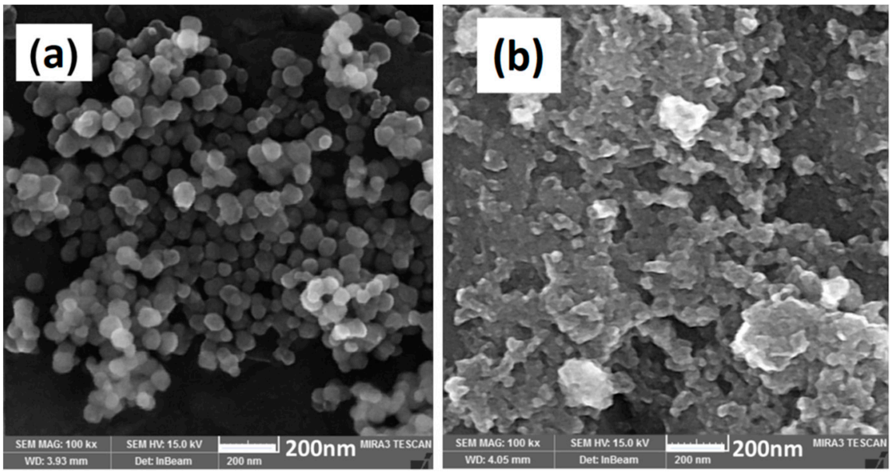

Figure 3. FE-SEM images of (**a**) PVC–MNPs and (**b**) Ni-doped PVC–MNPs [35,36].

FTIR spectra of the MNPs is presented in Figure 4. The intensities observed below 600 cm^{-1} are related to the stretching vibrations of Fe–O–Fe and/or Fe–O–Ni bonds [35,36]. The bands located at 2935 cm^{-1} and 2872 cm^{-1} are due to the asymmetric CH_2 stretching and symmetric CH_2 stretching of PVC, respectively. Furthermore, the IR bands located at 1472–75 cm^{-1} and 1250–5 cm^{-1} are corresponding to the C–H scissoring bending and CH_2 deformations, respectively. The observed peaks at 1190–5 cm^{-1} and 1165–8 cm^{-1} show C–C stretching and C–C bending, respectively. The peak at 960–5 cm^{-1} is $\nu_{bending}$ of CH (out-of-plane). The C–Cl bands of PVC can also be observed at 605–9 cm^{-1}, which prove the PVC grafting on the surface of the MNPs [35,36]. For both deposited PVC–MNPs and Ni-doped PVC–MNPs particles, there are IR bands which verified the presence of grafted PVC onto the Ni–MNPs particles.

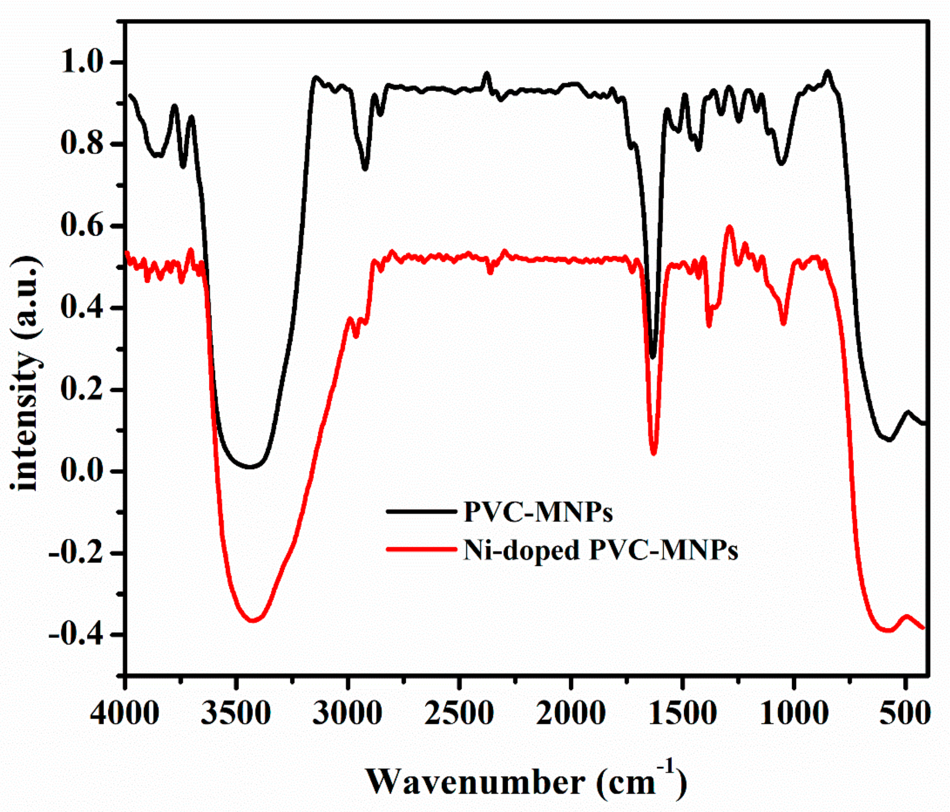

Figure 4. FT-IR spectra of the synthesized PVC–MNPs and Ni-doped PVC–MNPs.

Figure 5 shows the S-shaped VSM plots of MNPs demonstrating their superparamagnetic nature. The magnetic parameters including saturation magnetization (*Ms*), remanence (*Mr*) and coercivity (*Ce*) are extracted from the VSM plots and values of 43.72 emu/g, 0.11 emu/g and 0.5 Oe, are, respectively reported for PVC–MNPs in a previous work [35]. In the same order, *Ms* = 40.42 emu/g, *Mr* = 0.95 emu/g and *Ce* = 2.28 Oe are extracted for Ni^{2+}-doped PVC–MNPs, as reported previously [36]. The low *Ce* and trivial *Mr* are signatures of superparamagnetic nature of MNPs. Moreover, reduction in such values for Ni^{2+}-doped PVC–MNPs can be considered as a measure of successful surface functionalization of MNPs with PVC and Ni doping as well. However, the superparamagnetic nature of the MNPs was deteriorated by Ni-doping, as featured by increased *Ce* and *Mr*.

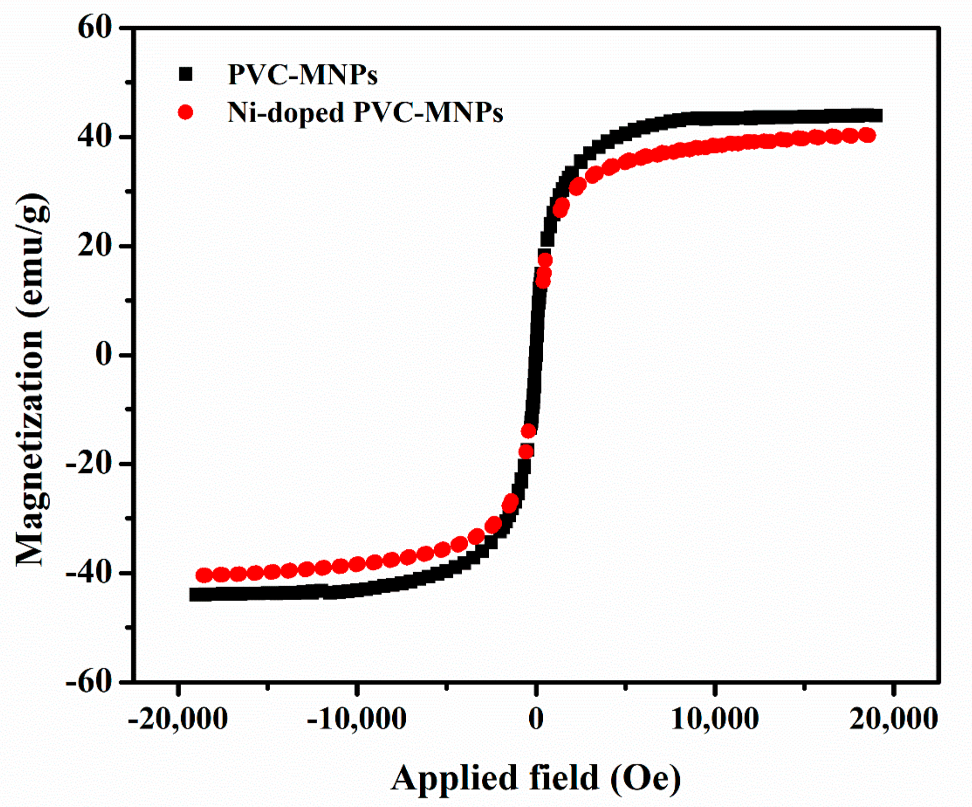

Figure 5. Vibrating sample magnetometry (VSM) curves of the synthesized PVC–MNPs and Ni-doped PVC–MNPs.

3.2. Cure Analysis

The curing potential of epoxy after incorporation of 0.1 wt% of the bare MNPs, PVC–MNPs and PVC/Ni-doped MNPs was analyzed by nonisothermal DSC at β of 5, 10, 15 and 20 °C/min (Figure 6). Addition of nanoparticles to epoxy did not change the curing mechanism of epoxy/amine system, which indicates that chemical reaction between epoxy and hardener dominantly derives the curing reaction [41]. On the other hand, addition of PVC–MNPs and PVC-Ni-doped MNPs changed the position of DSC thermograms.

At low heating rates, the curing moieties cannot efficiently participate in epoxide ring opening reaction due to lack of required level of kinetic energy per molecules [42]. Moreover, increases in the viscosity of the system expedited the gelation and vitrification, which results in deceleration of epoxy curing reaction [43]. By contrast, at high heating rate, the curing moieties have enough kinetics energy for curing process and can diffuse into epoxy network; therefore, easily attack the unreacted epoxy groups [44].

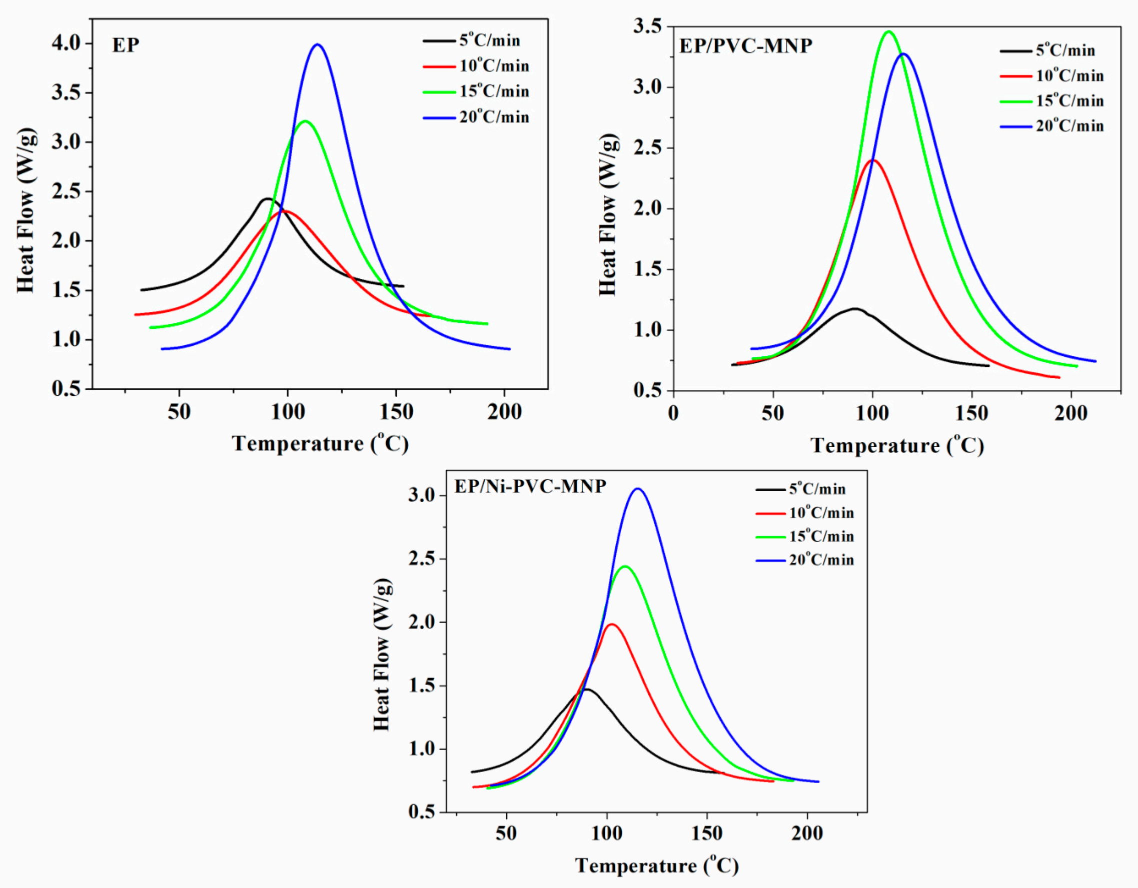

Figure 6. Nonisothermal DSC thermograms of EP, EP/PVC–MNPs [45] and EP/Ni-doped PVC–MNPs at different heating rates.

Cure parameters including the onset and the endset temperatures of the cure in DSC curves, respectively known as T_{onset} and T_{endset}, and the peak temperature (T_p) of DSC curves, the heat of cure and the width of curing temperature interval (ΔT) are summarized in Table 1.

As it is apparent from Table 1, both T_{onset} and T_p are shifted to higher temperatures by the introduction of PVC–MNPs or Ni-doped PVC–MNPs due to the steric hindrance of the nanoparticles. Overall, T_p was increased by increasing the heating rate that provided a narrower curing interval. By addition of PVC–MNPs or Ni-doped PVC–MNPs to the epoxy matrix, ΔT was significantly increased because of restricted chains mobility or expedition in the occurrence of vitrification that hardened interaction between the cure reactants [46]. Long PVC chains on the surface of MNPs could diffuse through the viscous media between the cross-linked network of epoxy to react with the remainder of epoxy rings [47]. Therefore, the PVC functional groups of MNPs surface accelerated the curing reaction at later stages of reaction where diffusion controls the crosslinking [48]. The total heat of reaction was increased as the PVC–MNPs added to the epoxy system; while it decreased by Ni-doped PVC–MNPs incorporation. The steric hindrance effect brought about by the Ni-doped PVC–MNPs expedited the occurrence of vitrification leading to a reduction in the values of ΔH_∞. Agglomeration of nanoparticles due to small number of PVC chains grafted on the surface of the Ni-doped MNPs at late stages if cure was also possible. As VSM results represented, the higher *Mr* and *Ce* values of Ni-doped PVC–MNPs suggests that these nanoparticles tend to agglomerate, which reduces the grafting efficiency of PVC on MNP surface. Ni dopants tend to position in the top layer of MNPs crystal, which dramatically increases the activity of MNPs surface [32]. High activity of the surface of Ni-doped MNPs keep the nanoparticles close to each other leading to less site of nanoparticles being accessible. Therefore, the PVC grafting yield was decreased that lowered the ΔH_∞ compared to PVC–MNP incorporated epoxy system.

Table 1. Cure parameters of the neat epoxy and its nanocomposites in terms of the rate of heating applied in nonisothermal DSC analyses. The neat epoxy and the epoxy containing PVC–MNPs were used as the control systems studied recently.

Sample Codes	β (°C/min)	T_{onset} (°C)	T_{endset} (°C)	T_p (°C)	ΔT (°C)	ΔH_∞ (J/g)
EP [45]	5	30.04	107.62	75.31	77.58	340.41
	10	29.70	165.3	98.4	135.7	319.40
	15	36.64	191.89	107.89	155.25	377.61
	20	38.62	146.67	96.09	108.05	374.39
EP/PVC–MNPs [45]	5	29.34	158.34	91.06	129.00	278.98
	10	32.07	193.94	100.17	161.86	513.07
	15	39.75	202.78	108.11	163.02	532.54
	20	39.04	212.07	115.47	173.03	387.40
EP/Ni-doped PVC–MNPs	5	32.72	158.48	90.06	125.76	354.05
	10	33.43	183.09	102.30	149.66	353.49
	15	40.38	192.87	108.96	152.50	339.31
	20	42.19	205.52	115.30	163.33	354.92

3.2.1. Qualitative Cure Analysis Based on *Cure Index*

Cure state of the epoxy nanocomposites can be evaluated by the use of *CI* as a dimensionless and simple criterion through the formula of: $CI = \Delta H^* \times \Delta T^*$, where $\Delta H^* = \Delta H_C / \Delta H_{Ref}$ and $\Delta T^* = \Delta T_C / \Delta T_{Ref}$. The parameters of ΔH_C and ΔH_{Ref} are the enthalpies of cure for the polymer composite and the reference sample (neat resin), respectively. In addition, the parameters of ΔT_C and ΔT_{Ref} are the total temperature range within which cure was completed for the polymer composite and the neat epoxy, respectively. The values of ΔT^*, ΔH^* and the *CI* were calculated and reported in Table 2. It was recently shown that the addition of bare MNPs and Ni-doped MNPs into epoxy resin leads to the poor cure state due to the agglomeration [24]. According to Table 2, at β of 5 and 10 °C/min when the curing moieties have enough time to react with each other the *CI* for the Ni-doped PVC–MNPs incorporated epoxy was good. However, at high β due to the lack of time the nanoparticles have no chance of interaction with cure moieties(characteristic of poor cure state). At high β, the potential of PVC groups on the surface of MNPs as well as the Ni in the Ni–MNPs for cure was higher because of high kinetic energy per molecule [49]. As it is apparent, EP/PVC–MNPs shows good cure state at heating rates of 10–20 °C/min with higher ΔH^* values compared to that of the EP/Ni-doped PVC–MNPs nanocomposite.

Table 2. Cure state parameters of samples.

Designation	β (°C/min)	ΔT^*	ΔH^*	*CI*	Quality
EP/PVC–MNPs [45]	5	1.66	0.82	1.36	**Poor**
	10	1.19	1.61	1.92	**Good**
	15	1.05	1.41	1.48	**Good**
	20	1.60	1.03	1.65	**Good**
EP/Ni–PVC–MNPs	5	1.62	1.04	1.68	**Good**
	10	1.10	1.11	1.22	**Good**
	15	0.98	0.90	0.88	**Poor**
	20	1.51	0.95	1.43	**Poor**

The VSM analysis can be used to explain this behavior as well as the effect of the bulk and surface modification of MNPs on epoxy crosslinking. The agglomeration of MNPs decreases the efficiency of nanoparticles in epoxy crosslinking due to their surface energy reduction. It can be concluded from VSM data that the surface modification of MNPs with PVC prevents agglomeration to some extent, as proved by lower *Ms* and *Mr* values for the assigned system indicating single domain centers for this nanoparticle. This is also observed in FESEM images (Figure 3).

3.2.2. Quantitative Cure Analysis

Cure Behavior

The extent of the curing reaction, α, was calculated as:

$$\alpha = \frac{\Delta H_T}{\Delta H_\infty}, \tag{1}$$

In the Equation (1), the ΔH_∞ and ΔH_T parameters are the total enthalpies of the complete cure reaction and the heat release up to the absolute temperature T, respectively. The variation of α by curing temperature at different heating rates for the neat epoxy [50,51] and epoxy nanocomposites containing PVC–MNP and Ni–PVC–MNP is presented in Figure 7. The S-shape of α curves seen for EP, EP/PVC–MNP and EP/Ni–PVC–MNP approves the autocatalytic mechanism behind the curing reaction. This indicates that the curing reaction is initiated by the reaction between epoxy and amine groups of curing agent until gelation occurred. At that time, at higher temperature the OH groups formed during the ring opening of epoxy participated in curing reaction through etherification reaction. Finally, the curing rate was slowed down by the occurrence of vitrification [52].

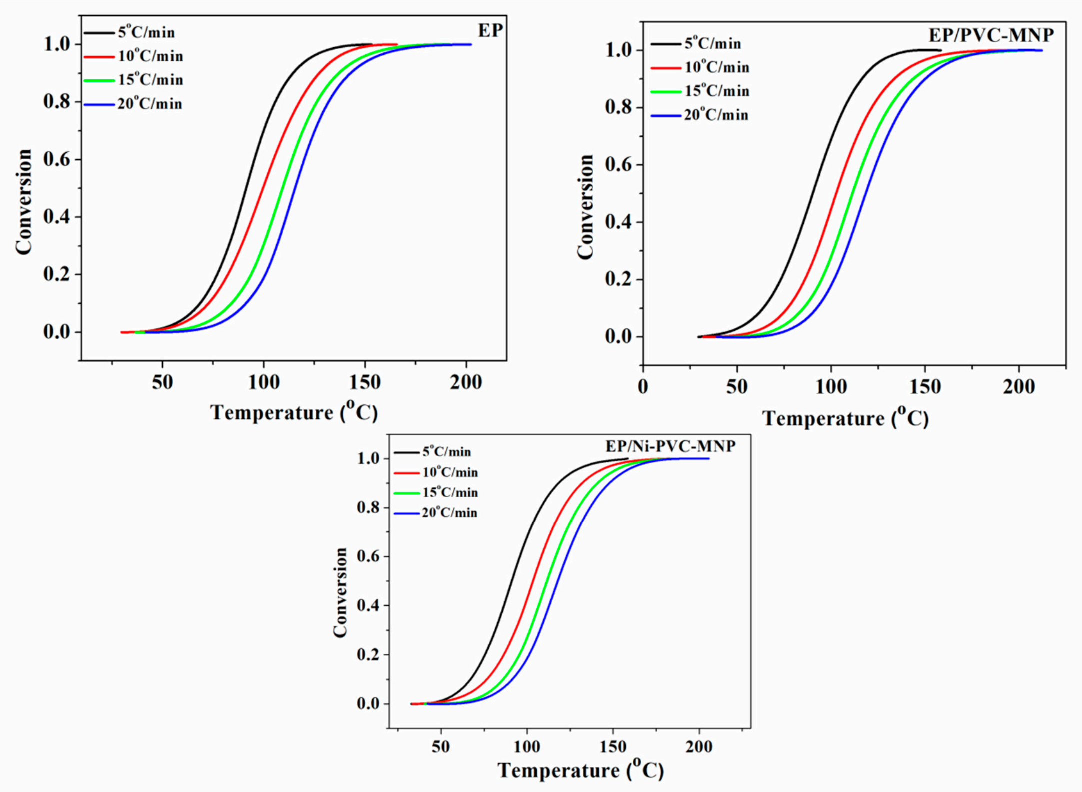

Figure 7. Variation of α as a function of reaction temperature for the EP (the reference sample) [50,51], EP/PVC–MNP and EP/Ni–PVC–MNP nanocomposites at heating rates of 5, 10, 15 and 20 °C/min.

Cure Kinetics

The rate of cure reaction can be obtained by using the following equation:

$$\frac{d\alpha}{dt} = k(T)f(\alpha), \tag{2}$$

In this equation, *f(α)* is the reaction model and *k(T)* indicates the reaction rate constant obtained from Arrhenius equation:

$$k(T) = Aexp(-\frac{E_{\alpha}}{RT}), \tag{3}$$

where *A*, *R* and *Eα* are the frequency factor, universal gas constant and activation energy of curing reaction, respectively. By substituting the relation of *k(T)* into Equation (2), the curing reaction rate can be rewritten as:

$$\frac{d\alpha}{dt} = Aexp(-\frac{E_{\alpha}}{RT})f(\alpha), \tag{4}$$

In order to estimate the reaction rate, the values of activation energy should be obtained. For this purpose, model-free isoconversional methods were used for calculating E_{α} as a function of temperature in a given *α* [53]. The well-known differential *Friedman* and the integral Kissinger–Akahira–Sunose (*KAS*) isoconversional methods were used for calculating E_{α} by Equations (5) and (6), respectively.

$$ln\left[\beta_i\left(\frac{d\alpha}{dT}\right)_{\alpha,i}\right] = ln[f(\alpha)A_{\alpha}] - \frac{E_{\alpha}}{RT_{\alpha,i}}, \tag{5}$$

$$ln\left(\frac{\beta_i}{T^2_{\alpha,i}}\right) = Const - 1.0008\left(\frac{E_{\alpha}}{RT_{\alpha}}\right), \tag{6}$$

The value of *Eα* as a function of *α* can be calculated from the slope of $ln\left[\beta_i(d\alpha/dT)_{\alpha,i}\right]$ vs. $1/T_{\alpha}$ (Equation (5)) and $ln\left(\beta_i/T^2_{\alpha,i}\right)$ vs. 1/T (Equation (6)) as shown in Figures A1 and A2 in Appendix A, respectively.

Figure 8 shows the variation of *Eα* with *α* obtained from *Friedman* and *KAS* models for EP, EP/PVC–MNP and EP/Ni–PVC–MNP nanocomposites. It is apparent from Figure 8 that the Eα values obtained from *Friedman* and *KAS* methods are almost alike. The variation of Eα values for EP, EP/PVC–MNP and EP/Ni–PVC–MNP nanocomposites in the α interval of $0.1 < \alpha < 0.9$ based on the differential *Friedman* and integral *KAS* models are indicative of the complexity of the curing processes or a complex kinetic behavior [54]. The decrease of Eα value at the late stage of curing reaction when the degree of conversion is high would be because of the autocatalytic nature of the reaction of epoxy with hardener. The decreasing of activation energy is due to the facilitation of autocatalytic ring opening fueled by the hydroxyl functional groups generated during the reaction [55]. In addition, by progress in curing reaction and formation of a partially cross-linked network, both the molecular weight and the viscosity of the system increase due to the restricted molecular mobility. It means that vitrification occurs and the curing reaction changes from the chemical crosslinking reaction to diffusion-controlled mechanism, which is responsible for the improvement of the reaction [56].

In the presence of PVC–MNP and Ni–PVC–MNP, the effective value of activation energy of the epoxy/amine system decreases due to the participation of functional groups on the surface of nanoparticles in curing reaction. PVC functional groups can attack the oxirane ring of epoxy resin with their Cl^- and lead to epoxide ring opening reaction, as schematically shown in Figure 9. This indeed results in lower values of activation energy. The long PVC chains on the surface of nanoparticles facilitate cure process, particularly when the reaction is under the control of diffusion [57]. It means that more functional groups (i.e., Cl^- and OH) are available for the unreacted epoxide rings, which makes the reaction easer and decrease the Eα.

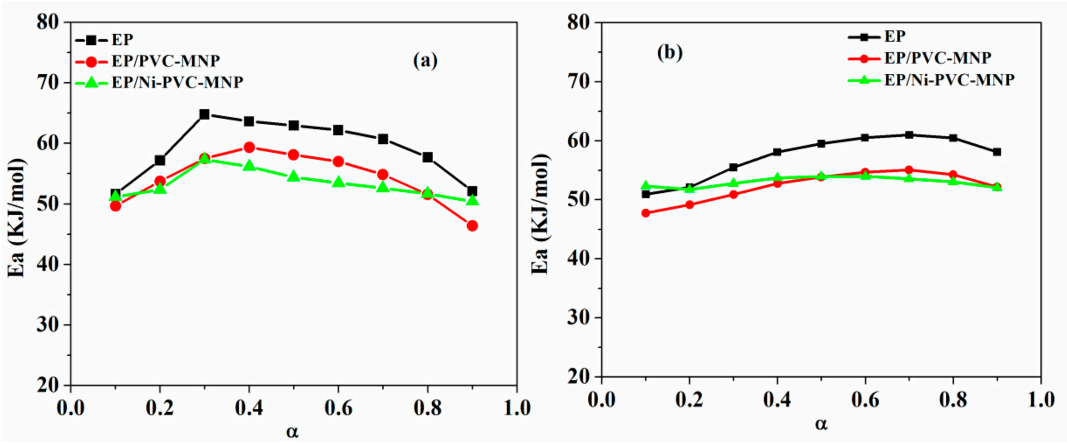

Figure 8. Variation of E_α for the EP (reference sample) [50,51] and EP/PVC–MNP and EP/Ni–PVC–MNP nanocomposites calculated by (**a**) *Friedman* and (**b**) *KAS* models.

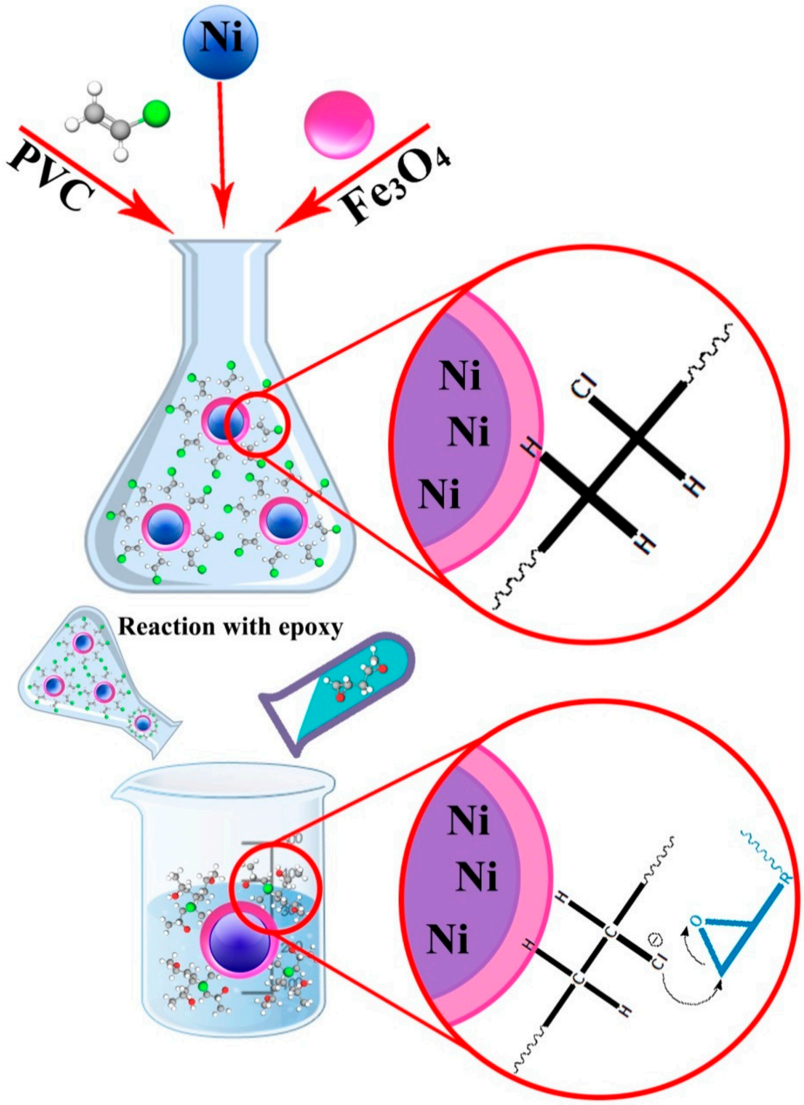

Figure 9. Possible reaction between PVC and epoxy ring.

Estimation of the Kinetics Model

In the next step, the reaction model of EP, EP/PVC–MNP and EP/Ni–PVC–MNP systems were determined by the use of the *Friedman* and Malek methods. The details of *Friedman* method and its mathematical relation can be found in Appendix B. Curing mechanism can also be estimated according to the Equation (A1) based on the shape of the plot of *ln[Af(α)]* vs. *ln(1-α).* Cross-linking reaction of the neat epoxy and its nanocomposites containing 0.1 wt% of PVC–MNP and Ni–PVC–MNP has an autocatalytic nature because of the maximum points being placed in the range of $0.2 < \alpha < 0.4$ that were derived from Figure A3.

A more accurate Malek method was also used for determination of kinetic model using maximum points of the Malek parameters of y(α) = (α_m), z(α) = ($\alpha_p{}^{\infty}$), which are defined in Equations (7) and (8), respectively and the conversion at the maximum point of DSC curves (α_p).

$$y(\alpha) = \left(\frac{d\alpha}{dt}\right)_{\alpha} exp\left(\frac{E_0}{RT_\alpha}\right) = Af(\alpha), \tag{7}$$

$$z(\alpha) = \left(\frac{d\alpha}{dt}\right)_{\alpha} T_\alpha^2, \tag{8}$$

$y(\alpha)$ and $z(\alpha)$ were normalized with respect to their maximum values to have values between 0 and 1. The variation of y(α) and $z(\alpha)$ for EP, EP/PVC–MNP and EP/Ni–PVC–MNP are shown in Figure 10 with respect to the theoretical master plots [58,59]. The values of α_m, α_p and $\alpha_p{}^{\infty}$ for the studied samples at different β are also reported in Table 3.

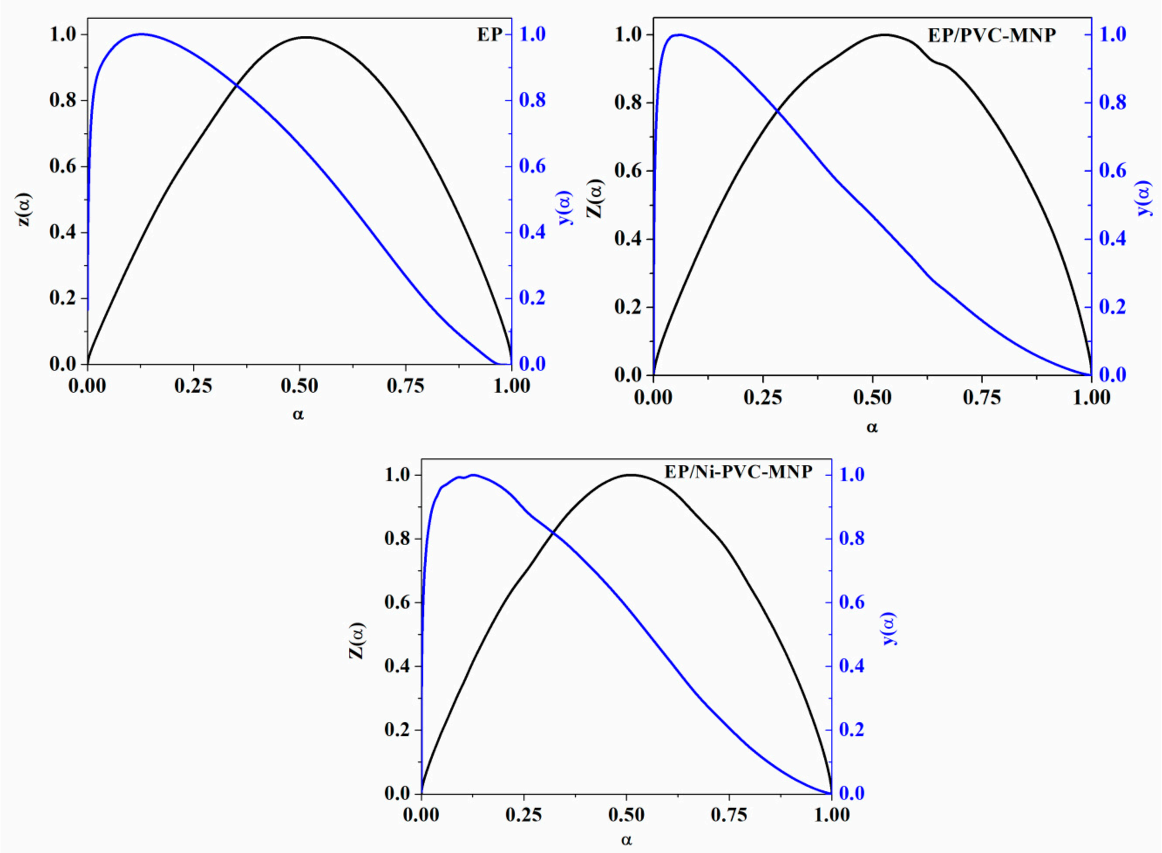

Figure 10. Values of Malek parameters (y(α) and $Z(\alpha)$) as a function of the extent of cure, α.

Table 3. Values of Malek parameters for the studied samples.

Designation	Heating Rate (°C/min)	$\alpha_p{}^{\infty}$	α_m	α_p
EP	5	0.487	0.144	0.512
	10	0.555	0.073	0.510
	15	0.418	0.236	0.498
	20	0.383	0.251	0.483
EP/PVC–MNP	5	0.505	0.061	0.527
	10	0.360	0.091	0.477
	15	0.357	0.084	0.467
	20	0.411	0.133	0.473
EP/Ni–PVC–MNP	5	0.491	0.126	0.510
	10	0.503	0.095	0.502
	15	0.475	0.093	0.481
	20	0.470	0.232	0.480

By comparing Figure 10 with Malek master plots and according to the data in Table 3 indicating that $\alpha_m < \alpha_p$ and $\alpha_p{}^{\infty}$ is higher than 0.632, the autocatalytic model was confirmed for EP, EP/PVC–MNP and EP/Ni–PVC–MNP.

Two-parameter autocatalytic kinetic model was defined by Sestak–Berggren as follows:

$$f(\alpha) = \alpha^m (1 - \alpha)^n, \tag{9}$$

where n and m are the orders of the non-catalytic and autocatalytic reaction, respectively.

Determination of the kinetics parameters

The values of the orders of reactions (n and m) and the frequency factor ($ln\ A$) were determined from Equations (A2) and (A3) in Appendix C (Table 4). In addition, the average value of activation energies ($\bar{E}\alpha$) for EP, EP/PVC–MNP and EP/Ni–PVC–MNP are reported in Table 4.

Table 4 suggests that both differential *Friedman* and the integral *KAS* models have quite reasonably confirmed each other. The overall order of the cure reaction ($m + n$) was higher than one in all systems, which make evident to the complexity of the curing reaction.

The addition of PVC–MNP or Ni–PVC–MNP nanoparticles to the epoxy matrix perturbs the autocatalytic reaction, as featured by a fall in the order of the autocatalytic reaction (m). Moreover, incorporation of PVC–MNP and Ni–PVC–MNP into epoxy confined the collisions between the curing components in the epoxy system, which reflected in lower value of *ln(A)* and consequently a lower activation energy.

Table 4. Kinetic parameters obtained from *Friedman* and *KAS* models.

Friedman

Designation	Heating Rate (°C/min)	$\bar{E}\alpha$ (kJ/mol)	ln(A) (1/s)	Mean (1/s)	m	Mean	n	Mean
EP	5	59.23	18.80	18.87	0.410	0.386	1.539	1.596
	10		18.56		0.139		1.439	
	15		18.98		0.445		1.678	
	20		19.12		0.551		1.727	
EP/PVC–MNP	5	54.25	16.74	17.06	0.192	0.341	1.429	1.618
	10		17.14		0.354		1.681	
	15		17.22		0.418		1.672	
	20		17.13		0.401		1.691	
EP/Ni–PVC–MNP	5	53.29	16.67	16.78	0.328	0.384	1.488	1.558
	10		16.79		0.388		1.560	
	15		16.84		0.407		1.587	
	20		16.83		0.414		1.598	

KAS

Designation	Heating rate (°C/min)	$\bar{E}\alpha$ (kJ/mol)	ln(A) (1/s)	Mean (1/s)	m	Mean	n	Mean
EP	5	57.35	18.18	18.27	0.430	0.406	1.523	1.579
	10		17.96		0.163		1.421	
	15		18.39		0.464		1.660	
	20		18.54		0.569		1.710	
EP/PVC–MNP	5	52.29	16.10	16.44	0.216	0.363	1.410	1.597
	10		16.51		0.375		1.659	
	15		16.61		0.438		1.651	
	20		16.53		0.421		1.669	
EP/Ni–PVC–MNP	5	53.01	16.58	16.69	0.331	0.387	1.485	1.556
	10		16.70		0.391		1.558	
	15		16.75		0.410		1.584	
	20		16.75		0.417		1.596	

Model validation

By obtaining kinetics parameters for EP, EP/PVC–MNP and EP/Ni–PVC–MNP systems, the conversion rate can be obtained accordingly:

$$\frac{d\alpha}{dt} = Aexp(-\frac{E_\alpha}{RT})\alpha^m(1-\alpha)^n, \tag{10}$$

Figure 11 compares the curing rate (dα/dt) obtained from Equation (10) and the one obtained from experiments at typical β of 5 °C.min^{-1}. Fortunately, the values of *dα/dt* calculated from the both *Friedman* and *KAS* models are in good agreement with experimental data.

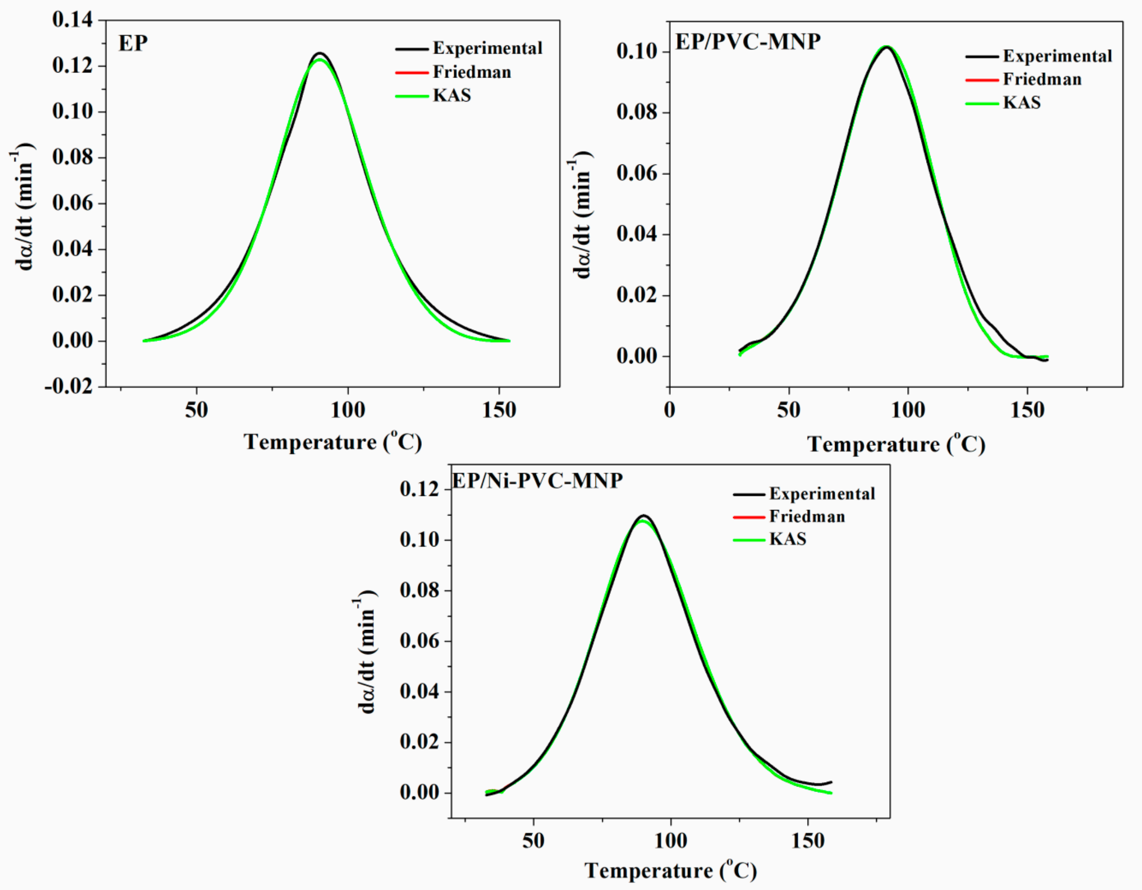

Figure 11. Typical of the experimental and the calculated rates of the cure reaction of the prepared samples at heating rate of 5 °C/min.

4. Conclusions

The cure behavior and kinetics of epoxy/MNPs nanocomposites strongly depends on the interaction between resin and nanoparticles. Moreover, bulk and surface treatment of MNPs can strongly improve the aforementioned interaction leading to increased cross-link density of epoxy network. Nonisothermal DSC analyses were carried out to study the potential of electrochemically synthesized PVC–MNPs and Ni-doped PVC–MNPs in epoxy curing reaction as a function of heating rate (β). It was found that at medium heating rates, where the kinetic energy per volume of system was adequate, the cure moieties had sufficient time for curing reaction, such that addition of 0.1 wt% of PVC–MNP increased the ΔH_{∞} from 319 and 377 for the neat epoxy to 513 and 532 J/g at β of 10 and 15 °C/min, respectively. It was ascribed to the Cl^{-} from PVC to the epoxide ring opening reaction. VSM data suggested that Ni-doped PVC–MNPs tend to agglomerate, which decreased the grafted amount of PVC on the surface was relatively high, as featured by high *Mr* value. Hence, Ni-doped PVC–MNPs hindered the curing reaction of epoxy at higher heating rates, as reflected in its poor cure state. Both *Friedman* and *KAS* isoconversional methods indicated lower values of activation energy for the epoxy system in the presence of PVC–MNP and Ni–PVC–MNP nanoparticles. A good confidence was observed between the experimental and the calculated values of the rate of cure reaction obtained by the *Friedman* and *KAS* methods.

Author Contributions: Conceptualization, M.R.S.; methodology, M.J. & M.R.G.; software, M.J. & Z.K.; validation, M.R.S.; formal analysis, M.J. & Z.K.; investigation, M.R. & B.B.; data curation, P.Z.; writing—original draft preparation, M.J.; writing—review and editing, A.M. & S.H.; supervision, M.R.G. & M.R.S. All authors have read and agreed to the published version of the manuscript.

Funding: This research received no external funding.

Conflicts of Interest: The authors declare no conflicts of interest.

Appendix A. Isoconversional Kinetic Methods

Appendix A.1. Friedman Model

By plotting $ln\left[\beta_i(d\alpha/dT)_{\alpha,i}\right]$ vs. $1/T_{\alpha}$ from Equation (5), the value of $E\alpha$ in a specific α can be calculated from the slope of Figure A1.

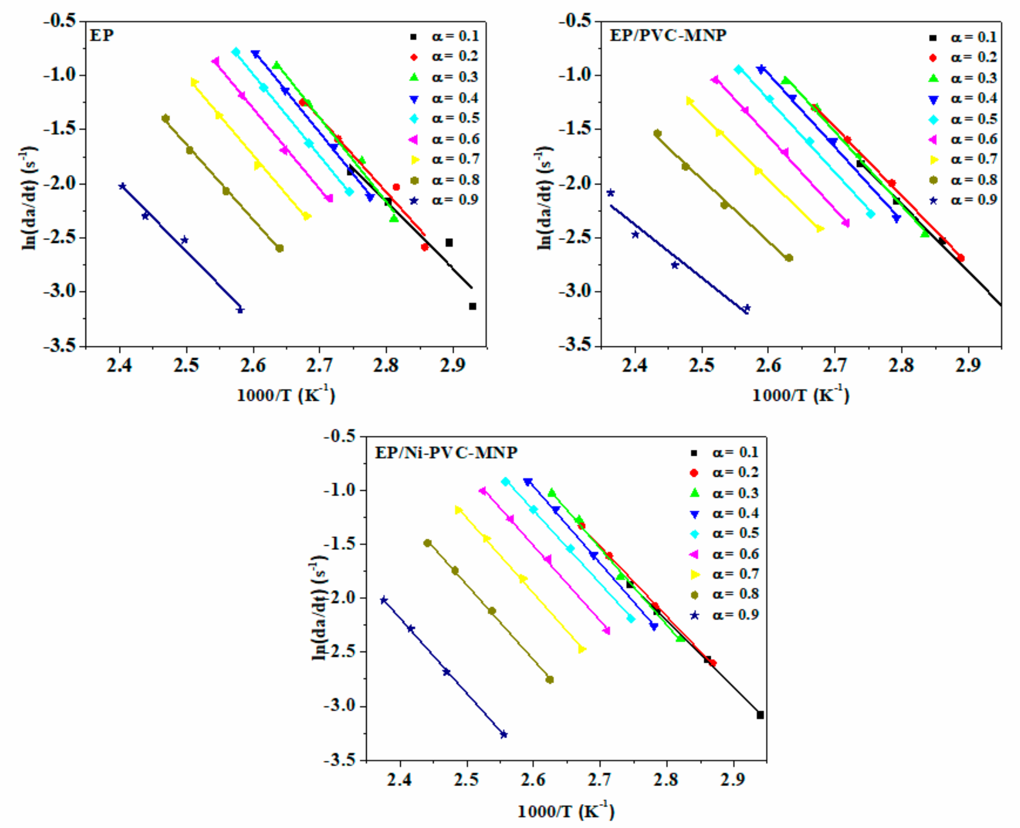

Figure A1. Fitting curves of *ln(dα/dt)* vs. 1/*T* based on *Friedman* model at β = 5 °C/min.

Appendix A.2. KAS Method

Plotting $ln\left(\beta_i/T^2_{\alpha,i}\right)$ vs. $1/T_{\alpha}$ from Equation (6) gives a straight line; such that its slop gives the activation energy at given α (Figure A2).

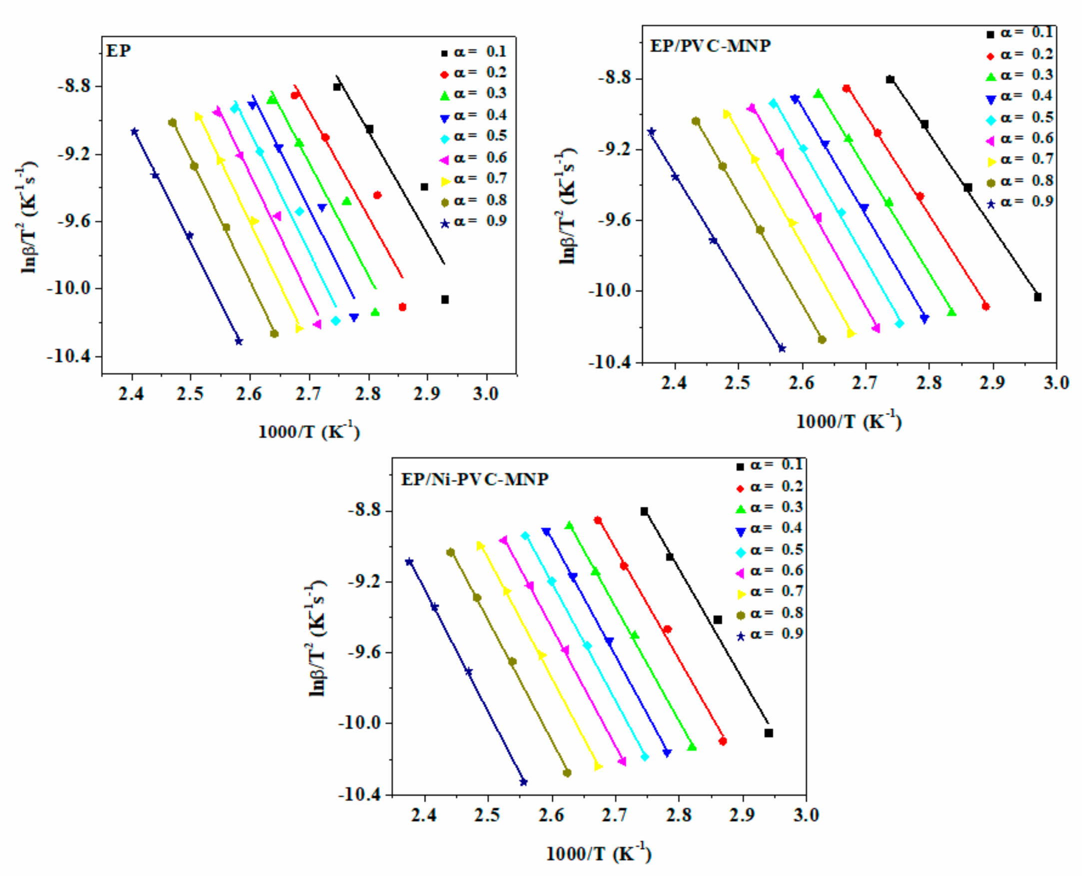

Figure A2. Fitting curves of $ln(\beta/T^2)$ vs. $1/T$ based on *KAS* model at $\beta = 5$ °C/min.

Appendix B. Selection of Curing Reaction Model

Appendix B.1. Friedman Model

The $f(\alpha)$ can be obtained from the *Friedman* method using Equation (A1). The shape of the plot of $ln[Af(\alpha)]$ vs. $ln(1-\alpha)$ denotes the autocatalytic or non-catalytic reaction mechanism (Figure A3).

$$ln[Af(\alpha)] = ln\left(\frac{d\alpha}{dt}\right) + \frac{E}{RT} = lnA + nln(1-\alpha), \tag{A1}$$

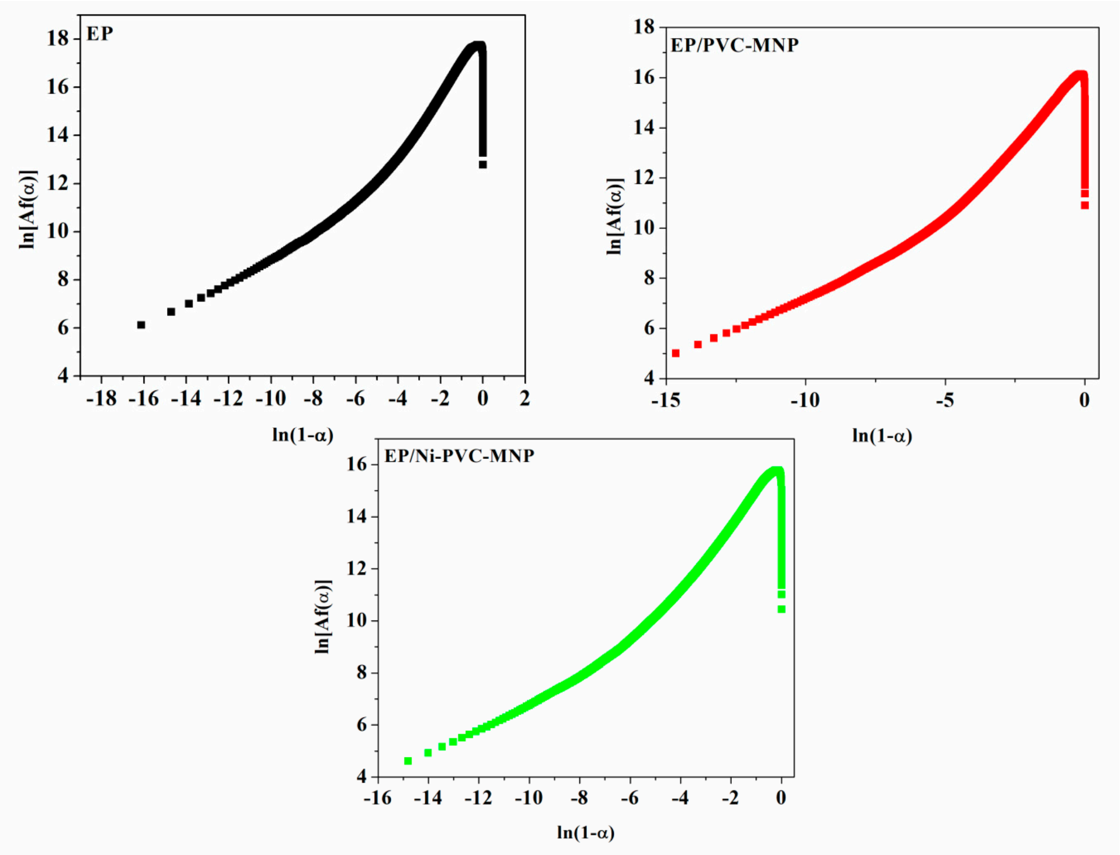

Figure A3. Curves of *ln [Af(α)]* vs. *ln*(1 − *α)* at 5 °C/min via *Friedman* method.

Appendix C. Determination of Degree of Reaction

The orders of curing reaction (n and m) and the frequency factor (A) are obtained by solving the following simultaneous differential equations:

$$ValueI = ln\left(\frac{d\alpha}{dt}\right) + \frac{E_\alpha}{RT} - ln\left[\frac{d(1-\alpha)}{dt}\right] - \frac{E_\alpha}{RT'} = (n-m)ln\left(\frac{1-\alpha}{\alpha}\right), \quad \text{(A2)}$$

$$ValueII = ln\left(\frac{d\alpha}{dt}\right) + \frac{E_\alpha}{RT} + ln\left[\frac{d(1-\alpha)}{dt}\right] + \frac{E_\alpha}{RT'} = (n+m)ln(\alpha-\alpha^2) + 2lnA, \quad \text{(A3)}$$

The slope of the plot of *ValueI* vs. $ln\ [(1-\alpha)/\alpha]$ (Figure A4) gives $(n-m)$, while the slope and the intercept of the plot of *ValueII* vs. $ln(\alpha-\alpha^2)$ (Figure A5) give the values of $(n+m)$ and $2lnA$.

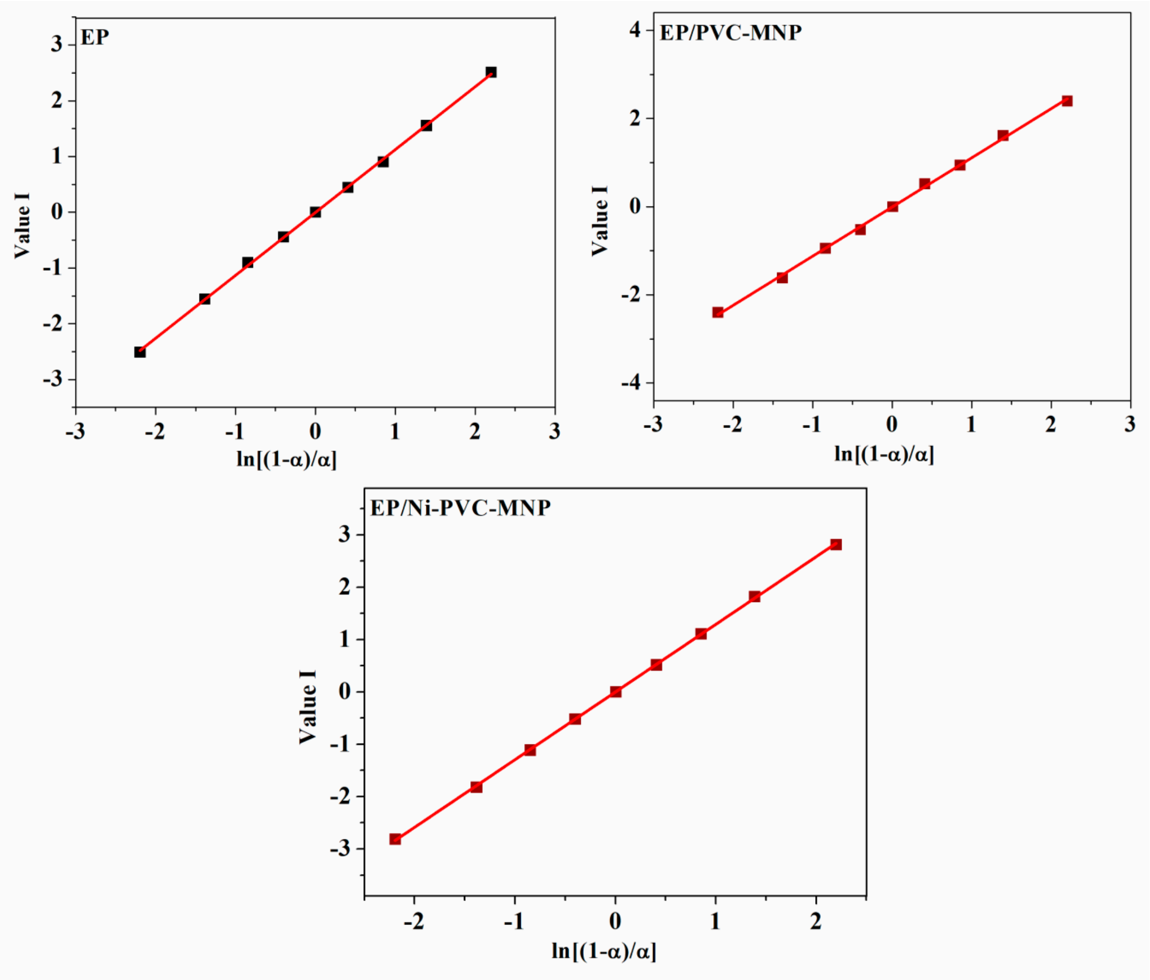

Figure A4. *Value I* of the samples at 5 °C/min.

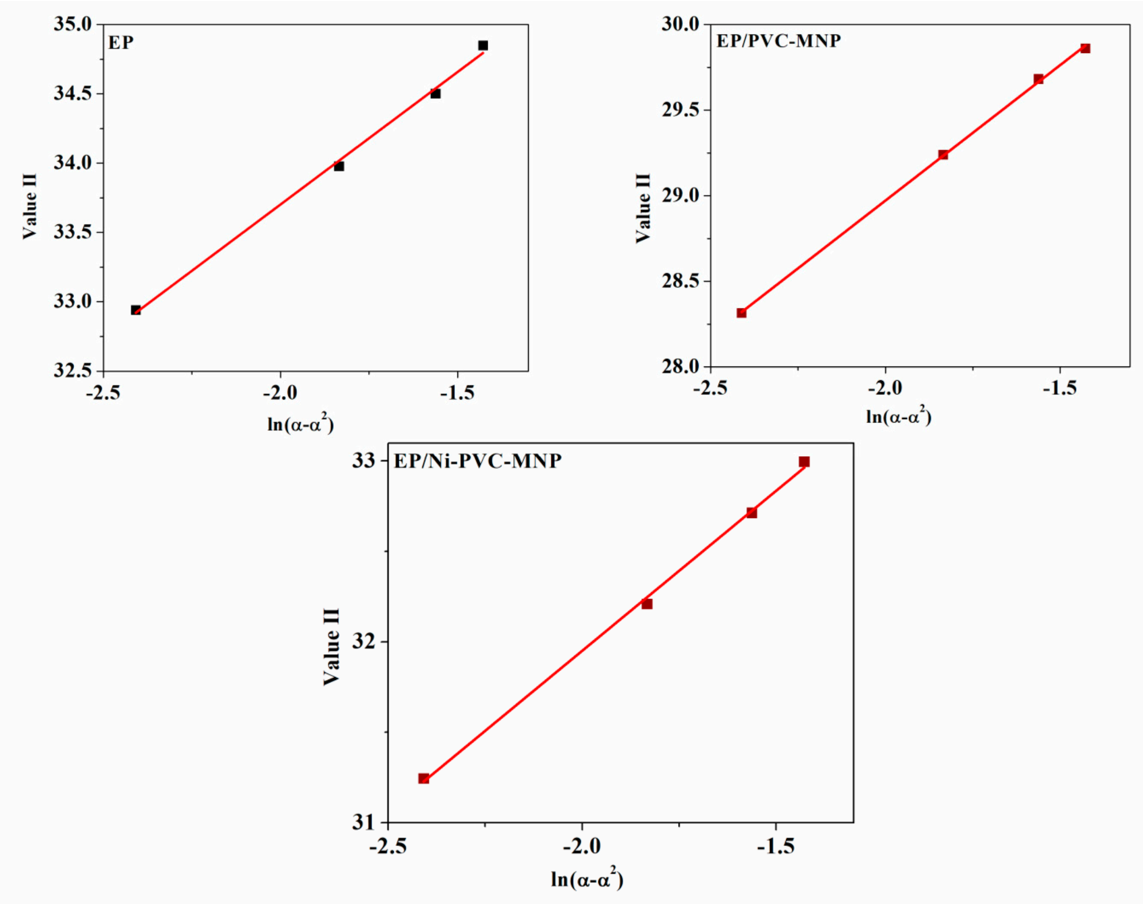

Figure A5. *Value II* of the samples at 5 °C/min.

References

1. Bisht, A.; Dasgupta, K.; Lahiri, D. Evaluating the effect of addition of nanodiamond on the synergistic effect of graphene-carbon nanotube hybrid on the mechanical properties of epoxy based composites. *Polym. Test.* **2020**, *81*, 106274. [CrossRef]
2. Jouyandeh, M.; Moini Jazani, O.; Navarchian, A.H.; Saeb, M.R. High-performance epoxy-based adhesives reinforced with alumina and silica for carbon fiber composite/steel bonded joints. *J. Reinf. Plast. Compos.* **2016**, *35*, 1685–1695. [CrossRef]
3. Jouyandeh, M.; Jazani, O.M.; Navarchian, A.H.; Shabanian, M.; Vahabi, H.; Saeb, M.R. Bushy-surface hybrid nanoparticles for developing epoxy superadhesives. *Appl. Surf. Sci.* **2019**, *479*, 1148–1160. [CrossRef]
4. Vahabi, H.; Jouyandeh, M.; Cochez, M.; Khalili, R.; Vagner, C.; Ferriol, M.; Movahedifar, E.; Ramezanzadeh, B.; Rostami, M.; Ranjbar, Z.; et al. Short-lasting fire in partially and completely cured epoxy coatings containing expandable graphite and halloysite nanotube additives. *Prog. Org. Coat.* **2018**, *123*, 160–167. [CrossRef]
5. Talo, A.; Passiniemi, P.; Forsen, O.; Yläsaari, S. Polyaniline/epoxy coatings with good anti-corrosion properties. *Synth. Met.* **1997**, *85*, 1333–1334. [CrossRef]
6. Saeb, M.R.; Najafi, F.; Bakhshandeh, E.; Khonakdar, H.A.; Mostafaiyan, M.; Simon, F.; Scheffler, C.; Mäder, E. Highly curable epoxy/MWCNTs nanocomposites: An effective approach to functionalization of carbon nanotubes. *Chem. Eng. J.* **2015**, *259*, 117–125. [CrossRef]
7. Jouyandeh, M.; Yarahmadi, E.; Didehban, K.; Ghiyasi, S.; Paran, S.M.R.; Puglia, D.; Ali, J.A.; Jannesari, A.; Saeb, M.R.; Ranjbar, Z.; et al. Cure kinetics of epoxy/graphene oxide (GO) nanocomposites: Effect of starch functionalization of GO nanosheets. *Prog. Org. Coat.* **2019**, *136*, 105217. [CrossRef]
8. Kornmann, X.; Lindberg, H.; Berglund, L.A. Synthesis of epoxy–clay nanocomposites: Influence of the nature of the clay on structure. *Polymer* **2001**, *42*, 1303–1310. [CrossRef]

9. Jouyandeh, M.; Jazani, O.M.; Navarchian, A.H.; Shabanian, M.; Vahabi, H.; Saeb, M.R. Surface engineering of nanoparticles with macromolecules for epoxy curing: Development of super-reactive nitrogen-rich nanosilica through surface chemistry manipulation. *Appl. Surf. Sci.* **2018**, *447*, 152–164. [CrossRef]
10. Akbari, V.; Najafi, F.; Vahabi, H.; Jouyandeh, M.; Badawi, M.; Morisset, S.; Ganjali, M.R.; Saeb, M.R. Surface chemistry of halloysite nanotubes controls the curability of low filled epoxy nanocomposites. *Prog. Org. Coat.* **2019**, *135*, 555–564. [CrossRef]
11. Karami, Z.; Jouyandeh, M.; Ali, J.A.; Ganjali, M.R.; Aghazadeh, M.; Maadani, M.; Rallini, M.; Luzi, F.; Torre, L.; Puglia, D.; et al. Cure Index for labeling curing potential of epoxy/LDH nanocomposites: A case study on nitrate anion intercalated Ni-Al-LDH. *Prog. Org. Coat.* **2019**, *136*, 105228. [CrossRef]
12. Karami, Z.; Jouyandeh, M.; Ali, J.A.; Ganjali, M.R.; Aghazadeh, M.; Paran, S.M.R.; Naderi, G.; Puglia, D.; Saeb, M.R. Epoxy/layered double hydroxide (LDH) nanocomposites: Synthesis, characterization, and Excellent cure feature of nitrate anion intercalated Zn-Al LDH. *Prog. Org. Coat.* **2019**, *136*, 105218. [CrossRef]
13. Karami, Z.; Jouyandeh, M.; Ali, J.A.; Ganjali, M.R.; Aghazadeh, M.; Maadani, M.; Rallini, M.; Luzi, F.; Torre, L.; Puglia, D.; et al. Development of Mg-Zn-Al-CO_3 ternary LDH and its curability in epoxy/amine system. *Prog. Org. Coat.* **2019**, *136*, 105264. [CrossRef]
14. Jouyandeh, M.; Tikhani, F.; Shabanian, M.; Movahedi, F.; Moghari, S.; Akbari, V.; Gabrion, X.; Laheurte, P.; Vahabi, H.; Saeb, M.R. Synthesis, characterization, and high potential of 3D metal–organic framework (MOF) nanoparticles for curing with epoxy. *J. Alloy. Compd.* **2020**, *829*, 154547. [CrossRef]
15. Wang, N.; Zhang, Y.; Chen, J.; Zhang, J.; Fang, Q. Dopamine modified metal-organic frameworks on anti-corrosion properties of waterborne epoxy coatings. *Prog. Org. Coat.* **2017**, *109*, 126–134. [CrossRef]
16. Jouyandeh, M.; Paran, S.M.R.; Shabanian, M.; Ghiyasi, S.; Vahabi, H.; Badawi, M.; Formela, K.; Puglia, D.; Saeb, M.R. Curing behavior of epoxy/Fe_3O_4 nanocomposites: A comparison between the effects of bare Fe_3O_4, Fe_3O_4/SiO_2/chitosan and Fe_3O_4/SiO_2/chitosan/imide/phenylalanine-modified nanofillers. *Prog. Org. Coat.* **2018**, *123*, 10–19. [CrossRef]
17. Jouyandeh, M.; Shabanian, M.; Khaleghi, M.; Paran, S.M.R.; Ghiyasi, S.; Vahabi, H.; Formela, K.; Puglia, D.; Saeb, M.R. Acid-aided epoxy-amine curing reaction as reflected in epoxy/Fe_3O_4 nanocomposites: Chemistry, mechanism, and fracture behavior. *Prog. Org. Coat.* **2018**, *125*, 384–392. [CrossRef]
18. Wang, L.; Qiu, H.; Liang, C.; Song, P.; Han, Y.; Han, Y.; Gu, J.; Kong, J.; Pan, D.; Guo, Z. Electromagnetic interference shielding MWCNT-Fe_3O_4@ Ag/epoxy nanocomposites with satisfactory thermal conductivity and high thermal stability. *Carbon* **2019**, *141*, 506–514. [CrossRef]
19. Huangfu, Y.; Liang, C.; Han, Y.; Qiu, H.; Song, P.; Wang, L.; Kong, J.; Gu, J. Fabrication and investigation on the Fe_3O_4/thermally annealed graphene aerogel/epoxy electromagnetic interference shielding nanocomposites. *Compos. Sci. Technol.* **2019**, *169*, 70–75. [CrossRef]
20. Saeb, M.R.; Bakhshandeh, E.; Khonakdar, H.A.; Mäder, E.; Scheffler, C.; Heinrich, G. Cure kinetics of epoxy nanocomposites affected by MWCNTs functionalization: A review. *Sci. World J.* **2013**, *2013*, 1–14. [CrossRef]
21. Jouyandeh, M.; Ganjali, M.R.; Ali, J.A.; Aghazadeh, M.; Stadler, F.J.; Saeb, M.R. Curing epoxy with electrochemically synthesized MnxFe$_3$-xO$_4$ magnetic nanoparticles. *Prog. Org. Coat.* **2019**, *136*, 105199. [CrossRef]
22. Jouyandeh, M.; Ali, J.A.; Aghazadeh, M.; Formela, K.; Saeb, M.R.; Ranjbar, Z.; Ganjali, M.R. Curing epoxy with electrochemically synthesized ZnxFe$_3$-xO$_4$ magnetic nanoparticles. *Prog. Org. Coat.* **2019**, *136*, 105246. [CrossRef]
23. Fu, Z.; Yang, B.; Zhang, Y.; Zhang, N.; Yang, Z. Dopant segregation and CO adsorption on doped Fe_3O_4 (1 1 1) surfaces: A first-principle study. *J. Catal.* **2018**, *364*, 291–296. [CrossRef]
24. Jouyandeh, M.; Ganjali, M.R.; Ali, J.A.; Aghazadeh, M.; Stadler, F.J.; Saeb, M.R. Curing epoxy with electrochemically synthesized NixFe$_3$-xO$_4$ magnetic nanoparticles. *Prog. Org. Coat.* **2019**, *136*, 105198. [CrossRef]
25. Jouyandeh, M.; Zarrintaj, P.; Ganjali, M.R.; Ali, J.A.; Karimzadeh, I.; Aghazadeh, M.; Ghaffari, M.; Saeb, M.R. Curing epoxy with electrochemically synthesized GdxFe$_3$-xO$_4$ magnetic nanoparticles. *Prog. Org. Coat.* **2019**, *136*, 105245. [CrossRef]
26. Jouyandeh, M.; Ganjali, M.R.; Ali, J.A.; Aghazadeh, M.; Stadler, F.J.; Saeb, M.R. Curing epoxy with electrochemically synthesized CoxFe$_3$-xO$_4$ magnetic nanoparticles. *Prog. Org. Coat.* **2019**, *137*, 105252. [CrossRef]

27. Jouyandeh, M.; Ganjali, M.R.; Ali, J.A.; Aghazadeh, M.; Saeb, M.R.; Ray, S.S. Curing epoxy with polyvinylpyrrolidone (PVP) surface-functionalized NixFe$_3$-xO$_4$ magnetic nanoparticles. *Prog. Org. Coat.* **2019**, *136*, 105259. [CrossRef]
28. Jouyandeh, M.; Ganjali, M.R.; Ali, J.A.; Aghazadeh, M.; Paran, S.M.R.; Naderi, G.; Saeb, M.R.; Thomas, S. Curing epoxy with polyvinylpyrrolidone (PVP) surface-functionalized ZnxFe$_3$-xO$_4$ magnetic nanoparticles. *Prog. Org. Coat.* **2019**, *136*, 105227. [CrossRef]
29. Jouyandeh, M.; Ali, J.A.; Akbari, V.; Aghazadeh, M.; Paran, S.M.R.; Naderi, G.; Saeb, M.R.; Ranjbar, Z.; Ganjali, M.R. Curing epoxy with polyvinylpyrrolidone (PVP) surface-functionalized MnxFe$_3$-xO$_4$ magnetic nanoparticles. *Prog. Org. Coat.* **2019**, *136*, 105247. [CrossRef]
30. Jouyandeh, M.; Ganjali, M.R.; Ali, J.A.; Aghazadeh, M.; Karimzadeh, I.; Formela, K.; Colom, X.; Cañavate, J.; Saeb, M.R. Curing epoxy with ethylenediaminetetraacetic acid (EDTA) surface-functionalized CoxFe$_3$-xO$_4$ magnetic nanoparticles. *Prog. Org. Coat.* **2019**, *136*, 105248. [CrossRef]
31. Jouyandeh, M.; Ganjali, M.R.; Ali, J.A.; Akbari, V.; Karami, Z.; Aghazadeh, M.; Zarrintaj, P.; Saeb, M.R. Curing epoxy with polyethylene glycol (PEG) surface-functionalized GdxFe$_3$-xO$_4$ magnetic nanoparticles. *Prog. Org. Coat.* **2019**, *137*, 105283. [CrossRef]
32. Jouyandeh, M.; Hamad, S.M.; Karimzadeh, I.; Aghazadeh, M.; Karami, Z.; Akbari, V.; Shammiry, F.; Formela, K.; Saeb, M.R.; Ranjbar, Z.; et al. Unconditionally blue: Curing epoxy with polyethylene glycol (PEG) surface-functionalized ZnxFe$_3$-xO$_4$ magnetic nanoparticles. *Prog. Org. Coat.* **2019**, *137*, 105285. [CrossRef]
33. Jouyandeh, M.; Karami, Z.; Ali, J.A.; Karimzadeh, I.; Aghazadeh, M.; Laoutid, F.; Vahabi, H.; Saeb, M.R.; Ganjali, M.R.; Dubois, P. Curing epoxy with polyethylene glycol (PEG) surface-functionalized NixFe$_3$-xO$_4$magnetic nanoparticles. *Prog. Org. Coat.* **2019**, *136*, 105250. [CrossRef]
34. Aghazadeh, M.; Ganjali, M.R. One-step electro-synthesis of Ni 2+ doped magnetite nanoparticles and study of their supercapacitive and superparamagnetic behaviors. *J. Mater. Sci. Mater. Electron.* **2018**, *29*, 4981–4991. [CrossRef]
35. Karimzadeh, I.; Dizaji, H.R.; Aghazadeh, M. Development of a facile and effective electrochemical strategy for preparation of iron oxides (Fe$_3$O$_4$ and γ-Fe$_2$O$_3$) nanoparticles from aqueous and ethanol mediums and in situ PVC coating of Fe$_3$O$_4$ superparamagnetic nanoparticles for biomedical applications. *J. Magn. Magn. Mater.* **2016**, *416*, 81–88. [CrossRef]
36. Aghazadeh, M.; Yavari, K. Galvanostatic Deposition of Magnetite Nanoparticles for Biomedical Applications: Simple Preparation and Surface Modification with Polyethylenimine and Polyvinyl Chloride. *Anal. Bioanal. Electrochem.* **2018**, *10*, 1426–1436.
37. Aghazadeh, M.; Karimzadeh, I. One-pot electro-synthesis and characterization of chitosan capped superparamagnetic Iron oxide nanoparticles (SPIONs) from ethanol media. *Curr. Nanosci.* **2018**, *14*, 42–49. [CrossRef]
38. Aghazadeh, M.; Karimzadeh, I.; Ganjali, M.R. Preparation of Nano-sized Bismuth-Doped Fe 3 O 4 as an Excellent Magnetic Material for Supercapacitor Electrodes. *J. Electron. Mater.* **2018**, *47*, 3026–3036. [CrossRef]
39. Aghazadeh, M.; Ganjali, M.R. Evaluation of supercapacitive and magnetic properties of Fe$_3$O$_4$ nano-particles electrochemically doped with dysprosium cations: Development of a novel iron-based electrode. *Ceram. Int.* **2018**, *44*, 520–529. [CrossRef]
40. Aghazadeh, M. One-step cathodic electrosynthesis of surface capped Fe$_3$O$_4$ ultra-fine nanoparticles from ethanol medium without using coating agent. *Mater. Lett.* **2018**, *211*, 225–229. [CrossRef]
41. Tikhani, F.; Moghari, S.; Jouyandeh, M.; Laoutid, F.; Vahabi, H.; Saeb, M.R.; Dubois, P. Curing Kinetics and Thermal Stability of Epoxy Composites Containing Newly Obtained Nano-Scale Aluminum Hypophosphite (AlPO$_2$). *Polymers* **2020**, *12*, 644. [CrossRef]
42. Ručigaj, A.; Kovačič, Ž.; Štirn, Ž.; Krajnc, M. The joint effect of amine and maleimide functional group in aminomaleimide on the curing kinetics and mechanical properties of epoxy resins. *Thermochim. Acta* **2020**, *690*, 178668. [CrossRef]
43. Xie, W.; Huang, S.; Tang, D.; Liu, S.; Zhao, J. Biomass-derived Schiff base compound enabled fire-safe epoxy thermoset with excellent mechanical properties and high glass transition temperature. *Chem. Eng. J.* **2019**, *394*, 123667. [CrossRef]
44. Boonlert-uthai, T.; Samthong, C.; Somwangthanaroj, A. Synthesis, thermal properties and curing kinetics of hyperbranched BPA/PEG epoxy resin. *Polymers* **2019**, *11*, 1545. [CrossRef] [PubMed]

45. Jouyandeh, M.; Ganjali, M.R.; Hadavand, B.S.; Aghazadeh, M.; Akbari, V.; Shammiry, F.; Saeb, M.R. Curing epoxy with polyvinyl chloride (PVC) surface-functionalized CoxFe$_3$-xO$_4$ nanoparticles. *Prog. Org. Coat.* **2019**, *137*, 105364. [CrossRef]
46. Jouyandeh, M.; Tikhani, F.; Hampp, N.; Yazdi, D.A.; Zarrintaj, P.; Ganjali, M.R.; Saeb, M.R. Highly curable self-healing vitrimer-like cellulose-modified halloysite nanotube/epoxy nanocomposite coatings. *Chem. Eng. J.* **2020**, *396*, 125196. [CrossRef]
47. Kieffer, A.; Hartwig, A. Interphase reaction of isocyanates with epoxy resins containing functional groups of different reactivity. *Macromol. Mater. Eng.* **2001**, *286*, 254–259. [CrossRef]
48. Rabearison, N.; Jochum, C.; Grandidier, J.-C. A cure kinetics, diffusion controlled and temperature dependent, identification of the Araldite LY556 epoxy. *J. Mater. Sci.* **2011**, *46*, 787–796. [CrossRef]
49. Ručigaj, A.; Alič, B.; Krajnc, M.; Šebenik, U. Curing of bisphenol A-aniline based benzoxazine using phenolic, amino and mercapto accelerators. *Express Polym. Lett.* **2015**, *9*, 647–657. [CrossRef]
50. Jouyandeh, M.; Karami, Z.; Hamad, S.M.; Ganjali, M.R.; Akbari, V.; Vahabi, H.; Kim, S.-J.; Zarrintaj, P.; Saeb, M.R. Nonisothermal cure kinetics of epoxy/ZnxFe$_3$-xO$_4$ nanocomposites. *Prog. Org. Coat.* **2019**, *136*, 105290. [CrossRef]
51. Jouyandeh, M.; Paran, S.M.R.; Khadem, S.S.M.; Ganjali, M.R.; Akbari, V.; Vahabi, H.; Saeb, M.R. Nonisothermal cure kinetics of epoxy/MnxFe$_3$-xO$_4$ nanocomposites. *Prog. Org. Coat.* **2020**, *140*, 105505. [CrossRef]
52. Van Assche, G.; Verdonck, E.; Van Mele, B. Interrelations between mechanism, kinetics, and rheology in an isothermal cross-linking chain-growth copolymerisation. *Polymer* **2001**, *42*, 2959–2968. [CrossRef]
53. Vyazovkin, S.; Burnham, A.K.; Criado, J.M.; Pérez-Maqueda, L.A.; Popescu, C.; Sbirrazzuoli, N. ICTAC Kinetics Committee recommendations for performing kinetic computations on thermal analysis data. *Thermochim. Acta* **2011**, *520*, 1–19. [CrossRef]
54. Song, Y.; Liu, M.; Zhang, L.; Mu, C.; Hu, X. Mechanistic interpretation of the curing kinetics of tetra-functional cyclosiloxanes. *Chem. Eng. J.* **2017**, *328*, 274–279. [CrossRef]
55. Akbari, V.; Jouyandeh, M.; Paran, S.M.R.; Ganjali, M.R.; Abdollahi, H.; Vahabi, H.; Ahmadi, Z.; Formela, K.; Esmaeili, A.; Mohaddespour, A. Effect of Surface Treatment of Halloysite Nanotubes (HNTs) on the Kinetics of Epoxy Resin Cure with Amines. *Polymers* **2020**, *12*, 930. [CrossRef] [PubMed]
56. Ratna, D. *Handbook of Thermoset Resins*; Ismithers: Shawbury, UK, 2009.
57. Corezzi, S.; Fioretto, D.; Santucci, G.; Kenny, J.M. Modeling diffusion-control in the cure kinetics of epoxy-amine thermoset resins: An approach based on configurational entropy. *Polymer* **2010**, *51*, 5833–5845. [CrossRef]
58. Gotor, F.J.; Criado, J.M.; Malek, J.; Koga, N. Kinetic analysis of solid-state reactions: The universality of master plots for analyzing isothermal and nonisothermal experiments. *J. Phys. Chem. A* **2000**, *104*, 10777–10782. [CrossRef]
59. Criado, J.; Malek, J.; Ortega, A. Applicability of the master plots in kinetic analysis of non-isothermal data. *Thermochim. Acta* **1989**, *147*, 377–385. [CrossRef]